Ultraspectral Imaging Based on Metasurfaces with Freeform Shaped Meta-Atoms

Jiawei Yang, Kaiyu Cui, Xusheng Cai, Jian Xiong, Hongbo Zhu, Shijie Rao, Sheng Xu, Yidong Huang,* Fang Liu, Xue Feng, and Wei Zhang*

Metasurfaces have an exceptional capacity to manipulate the phase, amplitude, polarization, or spectrum of light. However, unit cells, or meta-atoms, of metasurfaces are conventionally designed using regular shapes, limiting performance improvement. The utilization of metasurfaces with freeform shaped meta-atoms for on-chip ultraspectral imaging is proposed, where the freeform shaped patterns are generated with controllable feature sizes and boundary curvatures for feasible fabrication. These patterns broaden design diversity and enrich metasurface-unit spectral response with complicated Bloch modes, thus improving spectral imaging performance with enhanced spectrum recovery precision for broadband spectra and smaller center-wavelength deviation for narrowband spectra. A snapshot on-chip ultraspectral imaging, with 356 × 436 spectral pixels is experimentally demonstrated. Spectral resolution is state-of-the-art, at 0.5 nm, and mean fidelity of spectral reconstruction for a standard color board reaches 98.78%. These results support future applications in the field of precise intelligent perception. Moreover, the generating method for freeform shaped patterns also benefits for the forward and inverse designs for high-performance metasurfaces.

J. Yang, K. Cui, X. Cai, J. Xiong, H. Zhu, S. Rao, S. Xu, Y. Huang, F. Liu, X. Feng, W. Zhang
Department of Electronic Engineering
Tsinghua University
Beijing 100084, China
E-mail: kaiyucui@tsinghua.edu.cn; yidonghuang@tsinghua.edu.cn
J. Yang, K. Cui, X. Cai, J. Xiong, H. Zhu, S. Rao, S. Xu, Y. Huang, F. Liu, X. Feng, W. Zhang
Bejing National Research Center for Information Science and Technology (BNRist)
Tsinghua University
Beijing 100084, China
Y. Huang, W. Zhang
Bejing Academy of Quantum Information Science
Beijing 100084, China

1. Introduction

Metasurfaces are optically thin planar arrays of subwavelength scatterers, which can be designed to tailor the properties of light, such as phase,[1–5] amplitude,[6,7] polarization,[8–10] and spectrum.[11] Owing to their extraordinary functionalities, metasurfaces have been used in numerous applications including beam steering,[2] wave plates,[8] flat lenses,[5] holograms,[6,9] imaging,[12–15] and spectrometers.[16,17] In terms of metasurface design, the shapes and geometries of their unit cells, or meta-atoms, play an important role in light control. However, conventional designs are primarily based on parameterized regular-shaped meta-atoms, which conform to the shape of a circle,[2,4] rectangle,[3,7,18] square,[19] or ellipse,[9,11] and are subject to the physical intuition and experience of the designers. These cover only a small fraction of potential design possibilities. Although different types of shapes can be combined to expand the meta-atom library,[20] diversity of design is still limited. This limitation is also reflected in metasurface-based spectral imagers,[21–25] which are used to simultaneously acquire spectral and spatial information. Metasurfaces have been used as broadband filters with distinctive spectral response characteristics for computational spectrometers,[26] which enables spectral reconstruction over a wide wavelength range using a small number of filters compared with the narrowband filters,[27,28] and benefit from the complementary metal oxide semiconductor (CMOS) compatible fabrication process contrary to the miniaturized spectrometers based on quantum dots[29,30] or nanowire.[31,32] In contrast to the schemes of spectral imaging based on miniaturized dispersive optics[33,34] or interferometers,[35,36] metasurface-based approach boast the advantages of compact size, low cost, and snapshot manner without spatial scanning. However, it is difficult to improve both the spectral and spatial resolution of spectral imagers, based on existing metasurfaces with regular-shaped meta-atoms.

In this work, we propose a method for generating metasurfaces with freeform shaped meta-atoms by random assignment of grid values. Based on this, we demonstrate on-chip ultraspectral imaging and realize both high spectral and spatial resolution. Here, the spectrum of incident light is reconstructed from
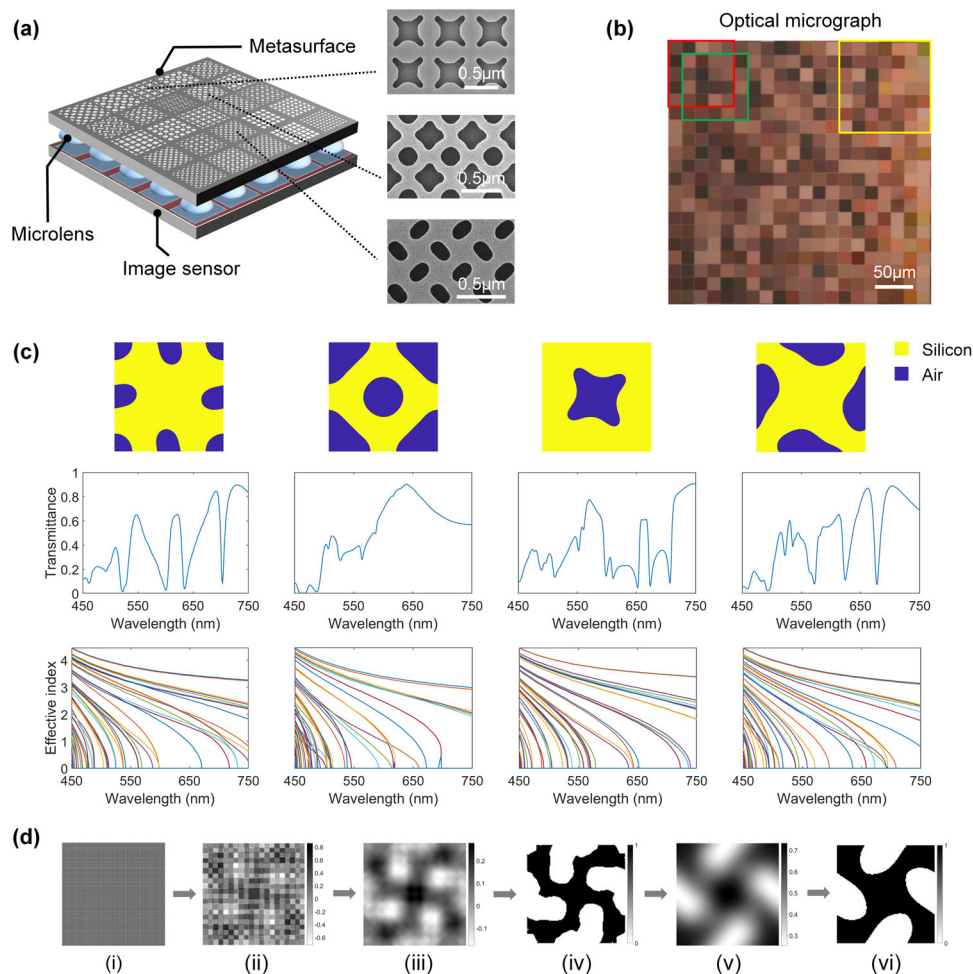
Figure 1. The proposed ultraspectral imager. a) The proposed ultraspectral imager consists of a metasurface layer, a microlens layer and an image sensor layer. In the metasurface layer, 356 × 436 micro-spectrometers may be formed by dynamically combining 5 × 5 metasurface units to form a spectral pixel. There are 400 types of metasurface units with distinctive freeform shaped meta-atoms. The scanning electron microscope images of three kinds of freeform shaped patterns are shown on the right-hand side. b) Optical micrograph of the fabricated 20 × 20 different metasurface units, each of which has a size of 17.58 μm × 17.58 μm covering 3 × 3 CMOS image sensor pixels. A micro-spectrometer can contain 5 × 5 units, as shown in the red/green boxes, 7 × 7 units in the yellow box, or other combinations, where adjacent spectral pixels could be overlapped. c) The transmission spectra and effective indices of the Bloch modes of four metasurface units with freeform shaped meta-atoms. d) The generation process of freeform shaped patterns including i) generation of fine grids, ii) random assignment of grid value, iii,iv) the first binarization process using a blurring filter and a thresholding function, and v,vi) the second binarization process.

detected light signals modulated by a certain number of freeform shaped metasurface units, and 356 × 436 spectral pixels (micro-spectrometers) are formed. We show that the light transmission characteristics of the metasurface units are significantly enriched, owing to the complicated scattering and coupling of diverse propagative Bloch modes in periodic freeform shaped patterns. Moreover, we employ simulations to verify that as minimum feature size decreases from 120 to 80 nm, the design diversity of the freeform shaped patterns increases, and the minimum relative mutual differences of 25 selected transmission spectra increase by ≈3 times. Based on the proposed metasurfaces with freeform shaped meta-atoms under the minimum feature size of 90 nm, we experimentally show that our device exhibits a 0.5-nm spectral resolution, which provides state-of-the-art performance in comparison to other works.[29–31] For the proposed device, the mean fidelity of spectral reconstruction for a standard color cal-

ibration board reaches 98.78%, showing promising potential for use in applications such as precision agriculture, food quality inspection, and object detection. In addition, the proposed method for generating freeform shaped patterns could also be used to build a pattern library for forward design, or in combination with deep learning techniques[37–42] for inverse design.

2. Results

2.1. Structure and Principle

The basic structure of the proposed ultraspectral imager is shown in **Figure 1**a, which is composed of a metasurface layer, a microlens layer, and an image sensor layer. The incident light is concentrated by the microlens array and converted into electric signals by the image sensor after passing through the metasurface

**ADVANCED
SCIENCE NEWS**

www.advancedsciencenews.com

LASER
& PHOTONICS
REVIEWS

www.lpr-journal.org

layer. There are a total of 158400 (360 × 440) metasurface units, with 400 different freeform shaped meta-atoms. Different metasurface units have distinctive spectral response functions $T_i(\lambda)$, and the input spectrum $f(\lambda)$ can be reconstructed from the detected signals I_i of the transmitted light by solving a system of linear equations:

$$I_i = \int_{\lambda_1}^{\lambda_2} T_i(\lambda)f(\lambda) + e_i \approx \sum_{j=1}^{M} T_i(\lambda_j)f(\lambda_j) + e_i, i = 1, \cdots, N \qquad (1)$$

where λ_1 and λ_2 define the operational wavelength range, and e_i represents the measurement noise. The target wavelength range is between 450 and 750 nm at a spacing of 0.5 nm ($M = 601$), so that through dynamically combining N metasurface units to form a spectral pixel (micro-spectrometer) by reusing all the metasurface units, an ultraspectral data cube of size 356 × 436 × 601 can be acquired with $N = 25$. The images of the scanning electron microscope of three types of freeform shaped patterns are shown at the side in Figure 1a. Figure 1b shows an optical micrograph of 20 × 20 different metasurface units with various colors. The size of each metasurface unit is designed to be 17.58 μm × 17.58 μm, which covers 3 × 3 pixels of CMOS image sensor (CIS) (the CIS pixel size is 5.86 μm) with the central pixel being the effective one since the surrounding pixels may be partially covered by the metasurface unit due to misalignment. For spectral imaging, the number of metasurface units in a micro-spectrometer N can be any positive value no more than 400, such as 5 × 5 or 7 × 7 denoted by the red, green, and yellow boxes in Figure 1b, respectively.

To decrease the size of each micro-spectrometer for a higher spatial resolution in the spectral imaging, N is typically less than the number of spectral channels of 601. Obtaining the spectrum from detected signals is therefore an underdetermined problem. Here, we graft dictionary learning and compression sensing techniques for spectral reconstruction[43,44] (see Section S1, Supporting Information). In addition, the mutual differences of the transmission spectra of the metasurface units inside one micro-spectrometer should be as large as possible to capture sufficient spectral information of the incident light. Freeform shaped meta-atoms are very effective in increasing the mutual differences in transmission spectra. The diverse spectral responses of freeform shaped patterns result from the complicated scattering and coupling of the propagative Bloch modes in the metasurface layer.[45,46] For clarity, we simulate the transmission spectra and effective refractive indices of the propagative Bloch modes for four metasurface units with different freeform shaped meta-atoms, using rigorous coupled-wave analysis (RCWA).[47] The results shown in Figure 1c indicate that the number and dispersion relations of the propagative Bloch modes vary with meta-atom shape, resulting in distinctive transmission spectra, i.e., spectral modulation characteristics. The physical scenarios are described as follows.

When light is incident on the imager from free space, it excites a finite number of propagating Bloch modes and an infinite number of evanescent Bloch modes of the metasurface units, owing to periodicity.[45,46] The propagating modes bounce back and forth many times inside the periodic structures, whereas the evanescent modes damp exponentially along the vertical direc-

tion, playing a negligible role in light transport. The transmitted light is strongly modulated in the spectral domain after passing through the metasurface layer because of the complicated scattering and coupling of these propagating Bloch modes at the substrate–metasurface interface.

The algorithm for generating the freeform shaped patterns is illustrated in Figure 1d. First, we generate a two-dimensional square grid (i). Second, different values are assigned to a coarse grid randomly obeying a certain distribution, for instance, the standard normal distribution. Moreover, certain geometric symmetries (e.g., C4-symmetry for polarization independence) are imposed on the pattern and transform the course grid to a fine one (ii). A blurring filter and a thresholding function are then employed to obtain the initial binary pattern, as shown in (iii and iv). Finally, another blurring and thresholding procedure is executed in (v and vi) to remove small features and smooth the edges of the pattern for feasible fabrication. In the final binary pattern, the area with a value of 1 corresponds to the dielectric material, whereas the area with a value of 0 represents air. In this process, the random values are assigned to the coarse grid instead of the fine grid directly, such that the pattern in (iv) will not be sporadic. Moreover, we obtain the feature sizes of the dielectric and air regions in the generated patterns by employing erosion and dilation operations, respectively. The boundary curvatures of the resulting patterns are related to the blurring parameters. A vast array of patterns with the desired feature sizes and boundary curvatures therefore can be obtained after post-selection, via the algorithm.

For the design of metasurface units, the above algorithm is first utilized to generate thousands of different shapes of meta-atoms that satisfy fabrication constraints, with a period varying from 300−750 nm in steps of 50 nm. In particular, the minimum feature size is set to 90 nm, considering practical fabrication precision in our case. In addition, the duty cycle varies from 0.1 to 0.9. We subsequently performed the simulation using RCWA and obtained the corresponding transmission spectra. Finally, we obtain 400 kinds of transmission spectra by maximizing their minimum relative mutual differences defined as $tor = \min_{i \neq j} \frac{1}{M} \sum_{k=1}^{M} |T_{ik} - T_{jk}|$, where T_{ik} is the kth element of the ith transmission spectrum vector with $M = 601$. In addition, we restrict all the periodic patterns to the C4-symmetric form for polarization–independent features.

2.2. Comparison with Regular Shapes

Theoretically, the number of freeform shaped patterns generated by our method is nearly infinite, in contrast to regular-shaped patterns. In practice, the constraint of minimum feature size places an upper limit on this number. We set different values for minimum feature size for different fabrication capabilities. For comparison, we simulate the transmission spectra of five groups of freeform, circle and regular-shaped periodic arrays with minimum feature sizes of 80, 90, 100, 110, and 120 nm. Here, the regular shapes include circle shape, square shape and cross shape used in ref. [23]. In these cases, the target wavelength range is 450−750 nm, with a 0.5-nm interval. For each group, 25 transmission spectra are selected by maximizing their minimum relative mutual difference tor, as shown in **Figure 2**a. It can be seen
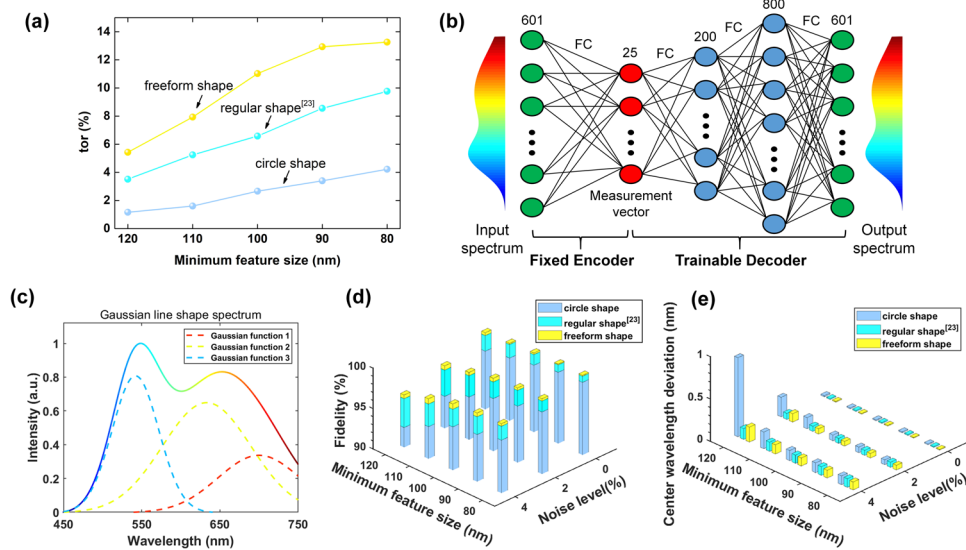
Figure 2. Comparison of freeform, circle and regular-shaped patterns. a) The minimum relative mutual difference of the 25 selected transmission spectra of freeform shaped, circle-shaped and regular-shaped patterns with minimum feature size from 120 to 80 nm. b) Schematic of the spectral encoder–decoder network, where the encoder is fixed with its connection weights corresponding to the transmission spectra of the metasurface units, and the decoder is trainable for spectral reconstruction. FC refers to a fully connected layer and the number represents the number of units in the corresponding layer. c) An example of a synthetic Gaussian line shape spectrum composed of three Gaussian distribution functions, as shown by dashed lines. d) Mean reconstruction fidelities of 200 000 synthetic spectra composed of Gaussian distribution functions, and e) the mean center-wavelength deviations for spectral reconstruction of 200 000 narrowband Gaussian spectra with a linewidth of 3 nm at various noise levels with 25 selected transmission spectra of freeform shaped, circle-shaped and regular-shaped patterns that have a minimum feature size from 120 to 80 nm.

that the *tor* for the freeform shaped patterns is significantly larger than that of the circle-shaped and regular-shaped patterns, and increases by ≈3 times when the minimum feature size decreases from 120 to 80 nm.

Furthermore, to evaluate performance in terms of the spectral reconstruction of selected transmission spectra under different minimum feature sizes, we construct a spectral encoder–decoder network, as depicted in Figure 2b. The network architecture is denoted as 601-FC-25-FC-200-LR-FC-800-LR-FC-601, where FC is a fully connected layer and LR represents leaky Rectified Linear Unit, with each number indicating the number of units in the corresponding layer. The encoder simulates the process of spectral measurement, that is, $I = Tf + e$, where f is the input spectrum, T is transmission spectra matrix, I is the output measurement vector, and e is the measurement noise vector. Therefore, the encoder consists of a fixed unbiased fully connected layer with its weighting matrix corresponding exactly to the matrix T.[48] Besides, we use Gaussian white noise as the simulated measurement noise, that is, $I = (1 + \sigma e_0)Tf$, where σ is the noise level and e_0 follows the standard normal distribution. The decoder is composed of three fully connected layers, playing the role of spectral reconstruction with the input measurement vector. For the reconstruction of broadband spectra, we use an input spectral dataset containing 200 000 synthetic Gaussian line shape spectra.[49] As illustrated in Figure 2c, the spectrum is produced by adding a series of Gaussian distribution component functions together. Finally, the height of each generated spectrum is normalized. We add Gaussian white noise at three different levels to the measurement vectors, and the results of the reconstruction fidelities are shown in Figure 2d. Here, fidelity is defined as $F(f_1, f_2) = \sum_{m=1}^{M} f_{1m} f_{2m}$, where f_1, f_2 are the normalized reference spectrum and recon-

structed spectrum, respectively, and f_{1m}, f_{2m} are the mth elements of f_1, f_2. As expected, the reconstruction fidelities for the freeform shaped patterns are significantly higher than those of the circle-shaped patterns, clearly higher than those of the regular-shaped patterns at various noise levels, and both increase with decreasing minimum feature size. For the spectral reconstruction of narrowband spectra, we use another input spectral dataset containing 200 000 Gaussian spectra with a linewidth of 3 nm. The peak location is randomly chosen from the range 460−740 nm, with a spacing of 0.5 nm, and the height was equal to 1. Similarly, we reconstruct the narrowband spectra at various noise levels. As illustrated in Figure 2e, the smaller minimum feature sizes also correspond to smaller center-wavelength deviations especially at a high noise level in practice, and freeform shaped patterns outperform the circle-shaped and regular-shaped patterns on the whole. Therefore, it is verified that the spectral recovery performance of freeform shaped metasurface units is better than that of regular-shaped units and could be further improved by reducing the minimum feature size.

2.3. Spectral Reconstruction Performance

To measure the performance of our device, transmission spectra of all metasurface units are calibrated. We then measure and reconstruct two broad-spectrum signals generated using a stack of colored plastic films. **Figure 3**a,b shows that the fidelities for the two broadband spectra are both above 99% even with 25 metasurface units ($N = 25$), and that fidelity increases as N increases. An explanation for this result is that as N is increased, more information regarding the unknown spectrum is acquired and the

**ADVANCED
SCIENCE NEWS**

www.advancedsciencenews.com
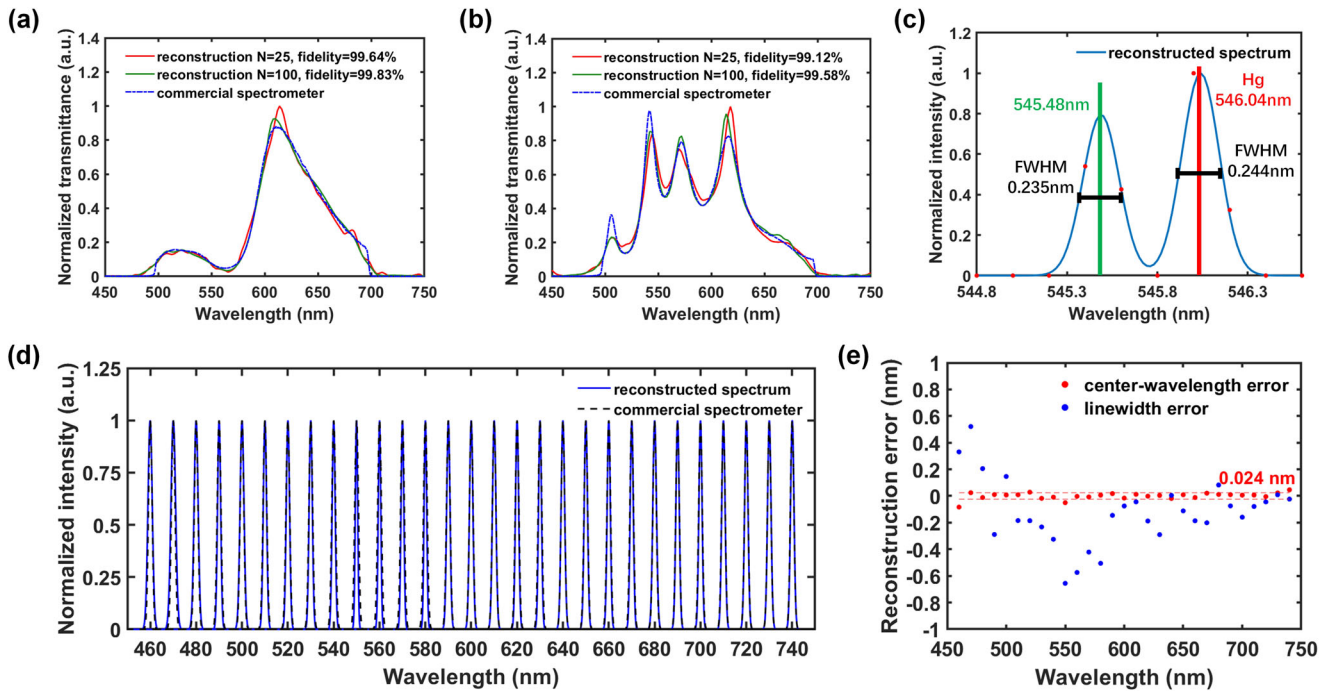
LASER
& PHOTONICS
REVIEWS

www.lpr-journal.org

Figure 3. Characterization of micro-spectrometers. a,b) Measurements of two broadband spectra using a micro-spectrometer with different *N* and the corresponding reference spectra obtained by a commercial spectrometer (OceanView QE Pro). c) Reconstructed spectrum of two narrow spectral lines with the 546-nm line from a mercury lamp and the 545.5-nm line from the monochromatic light source. We assume that the spectral lines have Gaussian line shapes. d) Reconstructed results for a series of narrowband spectra and comparison with the measurements of the commercial spectrometer. The peak positions range from 460 to 740 nm at a step of 10 nm. e) The reconstruction errors of the center-wavelength and linewidth for the results in (d), assuming Gaussian line shape.

problem of spectrum reconstruction becomes less underdetermined, resulting in improved accuracy for spectral reconstruction. In addition, we measure the spectral resolution using a mercury lamp and a tunable monochromatic light source, where a bandpass filter is used to block the other lines of mercury. Here, we recalibrate the transmission spectra with a wavelength spacing of 0.2 nm in the range of 543.6−546.6 nm. As shown in Figure 3c, by tuning the wavelength of the monochromatic light while maintaining the 546 nm line of mercury fixed, we demonstrate that the micro-spectrometer is able to resolve two peaks, separated by only ≈0.5 nm, which is better than the resolution of 0.8 nm in ref. [23]. To test the reconstruction performance for narrowband spectra, we measured monochromatic light sources with center wavelength ranging from 460 to 740 nm. The results in Figure 3d show that the reconstructed spectra closely match the measurements obtained by the commercial spectrometer (OceanView QE Pro). The standard deviation of the reconstruction errors for the center wavelength is merely 0.024 nm which outperforms the result of 0.04 nm in ref. [23], as shown in Figure 3e.

2.4. Ultraspectral Imaging Performance

The performance of snapshot ultraspectral imaging is demonstrated using the proposed device. As shown in **Figure 4**a, the metasurface layer with a size of 8 mm × 6.4 mm is integrated on top of a CIS (Thorlabs, CS235MU). Here, we use a 50-mm lens

with a fixed focal length (Thorlabs, MVL50M23) to form an image on the sensor. A 24-patch Macbeth color checker is used as the target, and the experiment is implemented under light from an ordinary fluorescent lamp. We choose *N* = 25 for each microspectrometer, and spatial multiplexing is utilized to enhance spatial resolution. For comparison, a commercial spectral camera (Dualix Instruments, GaiaField Pro V10) based on spatial scanning is used to capture the spectral image as a reference, and the color image in RGB form[50] is presented in Figure 4b. The recovered color image, which matches well with the reference results, is shown in Figure 4c. The reconstructed spectra (red lines) for all 24 colors with the references (blue lines) are shown in Figure 4d, where the subgraphs are arranged in an order consistent with the color blocks in Figure 4b,c. The spectra of the colors are recovered with mean fidelity of 98.78%, although certain colors such as gray, blue and purple are recovered with relatively lower fidelities due to the rather low signal-to-noise ratio for avoidance of overexposure. Overall performance could be further improved by expanding the wavelength range and increasing the dynamic range of the CIS.

Furthermore, in order to show the high spatial resolution for ultraspectral imaging using our device, the color chart is replaced with a plate of fruit, and the spectral imaging experiment is performed under the same conditions as before. As shown in **Figure 5**a, an ultraspectral data cube with 601 bands and 356 × 436 reconfigurable spectral pixels can be retrieved from the 12-bit raw image data captured by our device in a snapshot manner. The post-colored image converted from the data cube is also
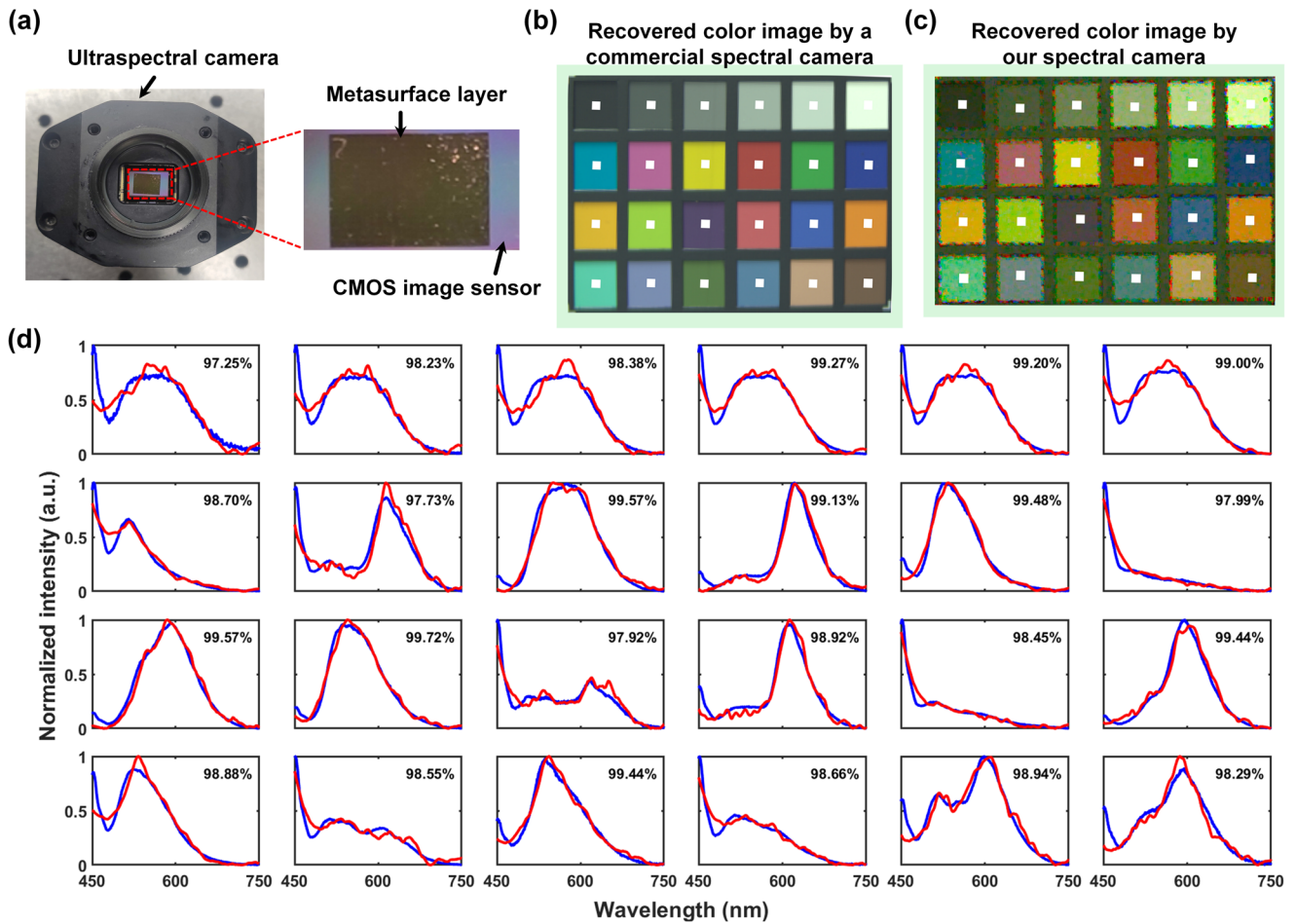
Figure 4. Snapshot ultraspectral imaging for a standard color chart. a) The ultraspectral camera has a metasurface layer (size 8×6.4 mm^2) integrated on a CMOS image sensor (Thorlabs, CS235MU). The recovered color image of a 24-patch Macbeth color chart obtained using b) a commercial spectral camera (Dualix Instruments, GaiaField Pro V10) and c) our ultraspectral camera. d) The reconstructed spectra (red lines) for the 24 types of color with the spectra captured by the commercial spectral camera as a reference (blue lines). The fidelities for the recovered spectra are marked in the top right-hand corner.
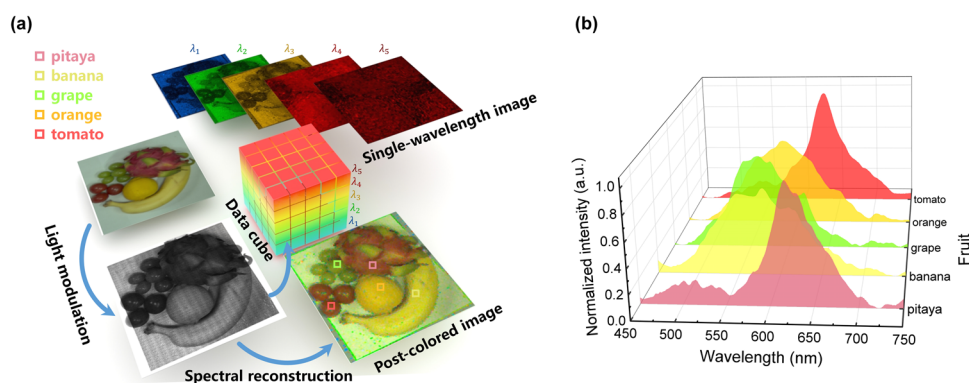

Figure 5. Snapshot ultraspectral imaging for a plate of fruit. a) A $356 \times 436 \times 601$ data cube of a spectral image of a plate of fruit is reconstructed from the metasurface-modulated raw image. The post-colored image in RGB form and images at five single wavelengths are shown. b) The reconstructed spectra of different fruits at the five corresponding sample positions in (a).

presented, which matches well with the ordinary color image. Here, an edge-detection technique is adopted to locally adjust the spectral reconstruction units to prevent jagged edges. Examples of single-wavelength images at 480, 530, 580, 630, and 680 nm are shown in Figure 5a. The recovered spectra of the five different fruits are shown in Figure 5b.

3. Conclusion

In this study, we demonstrate on-chip ultraspectral imaging based on metasurfaces with freeform shaped meta-atoms that are generated by our proposed algorithm, with controllable feature sizes and boundary curvatures. Through simulation and post-selection, we design 400 types of freeform shaped patterns that exhibit diverse spectral features originating from the complicated scattering and coupling of the propagative Bloch modes. In addition, we show that by decreasing the minimum feature size in the generation of freeform shaped patterns, the corresponding selected transmission spectra exhibit larger mutual differences and smaller spectral reconstruction errors. We experimentally demonstrate that our device exhibits excellent performance in terms of spectral imaging, with a state-of-the-art spectral resolution of 0.5 nm, a fidelity of spectral reconstruction for a standard color board of 98.78%, and a high spatial resolution of 356×436, which indicates that it may be used in various applications such as precision agriculture, food quality inspection, and object detection.

4. Experimental Section

Simulation and Design: The transmission spectra of metasurface units were simulated using RCWA, with air as the first layer, 220-nm c-Si metasurface as the second layer, and silicon dioxide as the substrate. The 400 freeform shaped patterns were post-selected by setting a proper low limit of relative mutual differences of their transmission spectra. By decreasing the low limit, more patterns can be selected and vice versa.

Generation of the Gaussian Spectrum Dataset: Each spectrum of the 200 000 synthetic Gaussian line shape spectra was produced by adding a series of Gaussian distribution component functions together, the number of which was generated by a geometric distribution with the probability parameter set to 0.3. For each component function, the peak location was a randomly chosen value from the range 450–750 nm, with a spacing of 0.5 nm, and the linewidth was randomly drawn from a uniform distribution in the range of 10 to 150 nm, and the height was randomly chosen in the interval (0, 1).

Device Fabrication: The ultraspectral imager was fabricated on a Silicon-On-Insulator wafer with a 220-nm Si layer. Metasurface units with freeform shaped meta-atoms were defined via electron beam lithography and transferred to the top silicon layer through inductively coupled plasma (ICP) etching. The silicon dioxide under the patterned metasurface was then removed by wet etching, using buffered hydrofluoric acid. Finally, the silicon metasurface layer was transferred onto a CIS chip using the poly-dimethylsiloxane transfer method (see Section S2, Supporting Information).

Calibration of Transmission Spectra: The transmission spectra of metasurface units under normal incidence using a 250-W tungsten-halogen lamp (Princeton Instruments, TS-428) as a broadband light source and a monochromator (Princeton Instruments, HRS-300) were measured. The wavelength of the light source from 450 to 750 nm at an interval of 0.5 nm and record all pixel values of the CIS was scanned. Then the ultraspectral imaging device with a commercial spectrometer (OceanView QE Pro) was replaced, the wavelength was scanned again, and the spectra of the

monochromatic light were recorded. From the measured spectrum under each wavelength, the corresponding light power density can be calculated via integration. In the end, the values of pixels under the metasurface units were corrected by dividing the calculated light intensities and the calibrated transmission spectra were obtained.

Supporting Information

Acknowledgements

Conflict of Interest

The authors declare no conflict of interest.

Author Contributions

J.Y. and K.C. conceived the study. K.C. and Y.H. supervised the project and provided much support on device fabrication and characterization. J.Y. designed the metasurface structures. J.Y., K.C., and Y.H. wrote the manuscript with contributions from all other co-authors. J.Y., J.X., H.Z., S.R., and S.X. participated in device characterization. J.Y., J.X., and S.R. participated in algorithm optimization. F.L., X.F., and W.Z. provided useful commentary on results. All authors read and approved the manuscript.

Data Availability Statement

The data that support the findings of this study are available from the corresponding author upon reasonable request.

Keywords

[1] S. M. Kamali, E. Arbabi, A. Arbabi, A. Faraon, *Nanophotonics* **2018**, *7*, 1041.

[2] R. A. Aoni, M. Rahmani, L. Xu, K. Zangeneh Kamali, A. Komar, J. Yan, D. Neshev, A. E. Miroshnichenko, *Sci. Rep.* **2019**, *9*, 6510.

[3] F. Yue, D. Wen, J. Xin, B. D. Gerardot, J. Li, X. Chen, *ACS Photonics* **2016**, *3*, 1558.

[4] Z. Lin, X. Li, R. Zhao, X. Song, Y. Wang, L. Huang, *Nanophotonics* **2019**, *8*, 1079.

[5] K. Chen, Y. Feng, F. Monticone, J. Zhao, B. Zhu, T. Jiang, L. Zhang, Y. Kim, X. Ding, S. Zhang, A. Alù, C.-W. Qiu, *Adv. Mater.* **2017**, *29*, 1606422.

[6] G.-Y. Lee, G. Yoon, S.-Y. Lee, H. Yun, J. Cho, K. Lee, H. Kim, J. Rho, B. Lee, *Nanoscale* **2018**, *10*, 4237.

[7] A. C. Overvig, S. Shrestha, S. C. Malek, M. Lu, A. Stein, C. Zheng, N. Yu, *Light: Sci. Appl.* **2019**, *8*, 92.

[8] F. Ding, Z. Wang, S. He, V. M. Shalaev, A. V. Kildishev, *ACS Nano* **2015**, *9*, 4111.

[9] A. Arbabi, Y. Horie, M. Bagheri, A. Faraon, *Nat. Nanotechnol.* **2015**, *10*, 937.

[10] M.-X. Ren, W. Wu, W. Cai, B. Pi, X.-Z. Zhang, J.-J. Xu, *Light: Sci. Appl.* **2017**, *6*, e16254.

[11] A. Tittl, A. Leitis, M. Liu, F. Yesilkoy, D.-Y. Choi, D. N. Neshev, Y. S. Kivshar, H. Altug, *Science* **2018**, *360*, 1105.

[12] D. Lee, M. Kim, J. Kim, H. Hong, T. Badloe, D. S. Kim, J. Rho, *Opt. Mater. Express, OME* **2019**, *9*, 3248.

[13] D. Lee, Y. Yang, G. Yoon, M. Kim, J. Rho, *Appl. Phys. Lett.* **2019**, *115*, 101102.

[14] D. Lee, J. Gwak, T. Badloe, S. Palomba, J. Rho, *Nanoscale Adv.* **2020**, *2*, 605.

[15] D. Lee, M. Kim, J. Rho, *Micromachines* **2021**, *12*, 1142.

[16] M. Faraji-Dana, E. Arbabi, A. Arbabi, S. M. Kamali, H. Kwon, A. Faraon, *Nat. Commun.* **2018**, *9*, 4196.

[17] Y. Ding, Y. Duan, X. Chen, X. Guo, X. Ni, *Conference on Lasers and Electro-Optics*. Optica Publishing Group **2020**, p. FTh4B.7.

[18] R. Zhao, X. Xiao, G. Geng, X. Li, J. Li, X. Li, Y. Wang, L. Huang, *Adv. Funct. Mater.* **2021**, *31*, 2100406.

[19] Q.-T. Li, F. Dong, B. Wang, F. Gan, J. Chen, Z. Song, L. Xu, W. Chu, Y.-F. Xiao, Q. Gong, Y. Li, *Opt. Express* **2016**, *24*, 16309.

[20] S. Shrestha, A. C. Overvig, M. Lu, A. Stein, N. Yu, *Light: Sci. Appl.* **2018**, *7*, 85.

[21] A. McClung, S. Samudrala, M. Torfeh, M. Mansouree, A. Arbabi, *Sci. Adv.* **2020**, *6*, 7646.

[22] F. Yesilkoy, E. R. Arvelo, Y. Jahani, M. Liu, A. Tittl, V. Cevher, Y. Kivshar, H. Altug, *Nat. Photonics* **2019**, *13*, 390.

[23] J. Xiong, X. Cai, K. Cui, Y. Huang, J. Yang, H. Zhu, Z. Zheng, S. Xu, Y. He, F. Liu, X. Feng, W. Zhang, *Optica* **2022**, *9*, 461.

[24] Z. Wang, S. Yi, A. Chen, M. Zhou, T. S. Luk, A. James, J. Nogan, W. Ross, G. Joe, A. Shahsafi, K. X. Wang, M. A. Kats, Z. Yu, *Nat. Commun.* **2019**, *10*, 1020.

[25] Y. Zhu, X. Lei, K. X. Wang, Z. Yu, *Photonics Res.* **2019**, *7*, 961.

[26] Z. Yang, T. Albrow-Owen, W. Cai, T. Hasan, *Science* **2021**, *371*, 0722.

[27] S.-W. Wang, C. Xia, X. Chen, W. Lu, M. Li, H. Wang, W. Zheng, T. Zhang, *Opt. Lett.* **2007**, *32*, 632.

[28] N. K. Pervez, W. Cheng, Z. Jia, M. P. Cox, H. M. Edrees, I. Kymissis, *Opt. Express* **2010**, *18*, 8277.

[29] J. Bao, M. G. Bawendi, *Nature* **2015**, *523*, 67.

[30] X. Zhu, L. Bian, H. Fu, L. Wang, B. Zou, Q. Dai, J. Zhang, H. Zhong, *Light: Sci. Appl.* **2020**, *9*, 73.

[31] Z. Yang, T. Albrow-Owen, H. Cui, J. Alexander-Webber, F. Gu, X. Wang, T.-C. Wu, M. Zhuge, C. Williams, P. Wang, A. V. Zayats, W. Cai, L. Dai, S. Hofmann, M. Overend, L. Tong, Q. Yang, Z. Sun, T. Hasan, *Science* **2019**, *365*, 1017.

[32] J. Meng, J. J. Cadusch, K. B. Crozier, *Nano Lett.* **2020**, *20*, 320.

[33] P. Cheben, J. H. Schmid, A. Delâge, A. Densmore, S. Janz, B. Lamontagne, J. Lapointe, E. Post, P. Waldron, D.-X. Xu, *Opt. Express* **2007**, *15*, 2299.

[34] S. Nezhadbadeh, A. Neumann, P. Zarkesh-Ha, S. R. J. Brueck, *Opt. Express* **2020**, *28*, 24501.

[35] A. V. Velasco, P. Cheben, P. J. Bock, A. Delâge, J. H. Schmid, J. Lapointe, S. Janz, M. L. Calvo, D.-X. Xu, M. Florjańczyk, M. Vachon, *Opt. Lett.* **2013**, *38*, 706.

[36] S. N. Zheng, J. Zou, H. Cai, J. F. Song, L. K. Chin, P. Y. Liu, Z. P. Lin, D. L. Kwong, A. Q. Liu, *Nat. Commun.* **2019**, *10*, 2349.

[37] J. Zhou, B. Huang, Z. Yan, J.-C. G. Bünzli, *Light: Sci. Appl.* **2019**, *8*, 84.

[38] W. Ma, F. Cheng, Y. Xu, Q. Wen, Y. Liu, *Adv. Mater.* **2019**, *31*, 1901111.

[39] G. Wetzstein, A. Ozcan, S. Gigan, S. Fan, D. Englund, M. Soljačić, C. Denz, D. A. B. Miller, D. Psaltis, *Nature* **2020**, *588*, 39.

[40] W. Ma, Z. Liu, Z. A. Kudyshev, A. Boltasseva, W. Cai, Y. Liu, *Nat. Photonics* **2020**, *15*, 77.

[41] Z. Liu, D. Zhu, S. P. Rodrigues, K.-T. Lee, W. Cai, *Nano Lett.* **2018**, *18*, 6570.

[42] Z. Liu, L. Raju, D. Zhu, W. Cai, *IEEE J. Emerg. Sel. Top. Circuits Syst.* **2020**, *10*, 126.

[43] J. Oliver, W. Lee, S. Park, H.-N. Lee, *Opt. Express* **2012**, *20*, 2613.

[44] J. Oliver, W.-B. Lee, H.-N. Lee, *Opt. Express* **2013**, *21*, 3969.

[45] P. Lalanne, J. P. Hugonin, P. Chavel, *J. Lightwave Technol.* **2006**, *24*, 2442.

[46] V. Karagodsky, C. J. Chang-Hasnain, *Opt. Express* **2012**, *20*, 10888.

[47] J.-P. Hugonin, P. Lalanne, Light-in-Complex-Nanostructures/RETICOLO, V9, Zenodo, **2021**.

[48] H. Song, Y. Ma, Y. Han, W. Shen, W. Zhang, Y. Li, X. Liu, Y. Peng, X. Hao, *Adv. Theory Simul.* **2021**, *4*, 2000299.

[49] C. Kim, D. Park, H.-N. Lee, *Sensors* **2020**, *20*, 594.

[50] T. Smith, J. Guild, *Trans. Opt. Soc.* **1931**, *33*, 73.